

Mitigation of mineral scaling in membrane capacitive deionization – Understanding the role of pH changes and carbonates

Antony Cyril Arulrajan^{a,b}, Min-Chen Wu^c, Slawomir Porada^{d,b}, Jouke E. Dykstra^{a,*}, Chia-Hung Hou^c, Albert van der Wal^a

^a Environmental Technology, Wageningen University & Research, Bornse Weilanden 9, 6708 WG, Wageningen, the Netherlands

^b Wetsus, European Centre of Excellence for Sustainable Water Technology, Oostergoweg 9, 8911 MA Leeuwarden, the Netherlands

^c Graduate Institute of Environmental Engineering, National Taiwan University, No.1, Sec. 4, Roosevelt Rd., Taipei 10617, Taiwan

^d Department of Process Engineering and Technology of Polymeric and Carbon Materials, Wrocław University of Science and Technology, Wyb. Wyspińskiego 27, 50-370 Wrocław, Poland

ARTICLE INFO

Editor: Xing Yang

Keywords:

Membrane capacitive deionization
pH changes
Dissolved inorganic carbon
Mineral scaling
Ion-exchange membrane

ABSTRACT

Mineral scaling in water desalination is caused by the precipitation of salts, which is affected by various factors such as the presence of specific ions, solution pH, and temperature. While extensively researched in technologies like reverse osmosis (RO), understanding mineral scaling in membrane capacitive deionization (MCDI) remains limited. During MCDI operation, the pH of the effluent fluctuates, potentially triggering mineral scaling. The present study investigates how the adsorption and desorption of HCO_3^- ions and the distribution of dissolved inorganic carbon (DIC) species (H_2CO_3 , HCO_3^- , and CO_3^{2-}) drive pH changes. We examine mineral scaling formation at various water recoveries during MCDI operation using different thicknesses of the anion exchange membrane (AEM). Our findings indicate that pH changes increase with higher water recoveries and that increasing the AEM thickness provides a pathway to enhance MCDI stability, consequently lowering the need for anti-scaling agents.

1. Introduction

Desalination technologies play a vital role in addressing water scarcity issues by producing fresh water, particularly in regions with limited access to natural freshwater sources [1–3]. Desalination processes remove salt ions from the source water employing various driving forces including temperature, pressure, or electrical potential differences [4–9]. For instance, in thermal desalination methods such as multi-effect distillation (MED), the feed water undergoes vaporization, and upon condensation, purified water is obtained, while the salt is left behind in the concentrate [7,10]. Reverse osmosis (RO) and nanofiltration (NF) techniques involve the passage of water through semi-permeable membranes under pressure, separating desalinated water from a concentrated stream rich in salt ions [4,11–15]. In membrane capacitive deionization (MCDI) and electrodialysis (ED), an electrical potential difference is applied to extract salt ions from saline water, generating desalinated water and concentrate [8,9,16]. Despite their differences, all these technologies share a common challenge: the concentration of ions in the concentrate is higher than in the feed water,

posing a potential risk of mineral scaling.

In the context of MCDI, various factors influence mineral scaling, including salt solubility limits, ion types, and solution pH [5,10,17,18]. Particularly noteworthy is the impact of hardness ions such as Ca^{2+} and Mg^{2+} , as they tend to precipitate as carbonate, sulfate, or phosphate salts, resulting in mineral scaling in MCDI systems. Mineral scaling in MCDI can impact long-term salt removal efficiency and energy consumption, leading to increased operational costs and greater reliance on anti-scaling agents [8,11,12,19,20]. Despite numerous strategies proposed to mitigate scaling in conventional desalination methods such as RO and MED, understanding and controlling scaling in MCDI remain limited [13,17].

An MCDI cell consists of two porous carbon electrodes (an anode and a cathode), two ion-exchange membranes (IEMs) (an anion exchange membrane (AEM) positioned in front of the anode and a cation exchange membrane (CEM) in front of the cathode), and a porous spacer material used to separate the electrodes and facilitate water flow during operation. The MCDI cell is alternately charged to adsorb ions, resulting in the production of desalinated water, and discharged to desorb ions,

* Corresponding author.

E-mail address: jouke.dykstra@wur.nl (J.E. Dykstra).

<https://doi.org/10.1016/j.jwpe.2024.105094>

Received 30 November 2023; Received in revised form 1 February 2024; Accepted 29 February 2024

Available online 12 March 2024

2214-7144/© 2024 The Author(s). Published by Elsevier Ltd. This is an open access article under the CC BY license (<http://creativecommons.org/licenses/by/4.0/>).

resulting in the production of a concentrate solution (Fig. 1a). Throughout MCDI's cyclic operation, noticeable pH fluctuations are observed in the effluent, as shown in Fig. 1b. Notably, the discharge phase yields a higher pH than the feedwater. This pH elevation during discharge triggers mineral scaling, underscoring the importance of understanding the underlying mechanisms behind these pH changes. Such insights are essential for improving the long-term stability of MCDI systems.

Earlier studies of pH fluctuations in MCDI systems postulated that such changes originated from faradaic processes like water splitting, carbon oxidation, and the generation of Cl_2 gas. However, there are also studies indicating theoretically and experimentally that non-faradaic processes, such as water dissociation because of disparities in ion transport rates, can also contribute to pH alterations [21–24]. As MCDI cells undergo numerous desalination cycles, the electrodes gradually age, diminishing the significance of faradaic reactions like carbon oxidation due to the depletion of available carbon groups for oxidation. Consequently, non-faradaic processes emerge as the primary cause of pH changes [25].

In our previous work using aged electrodes, we have shown that pH fluctuations in brackish water desalination stem from the adsorption and desorption of bicarbonate ions (HCO_3^-). During charging, HCO_3^- ions are adsorbed, resulting in a decrease in effluent pH. Conversely, discharge results in the desorption of HCO_3^- ions, leading to a rise in effluent pH. When the concentrations of ions such as Ca^{2+} and HCO_3^- increase, mineral scaling may also exacerbate as these ions can precipitate as CaCO_3 salt [25].

Previous studies on mineral scaling in MCDI have clarified that scaling primarily occurs on the membranes and the spacer channel, with minimal impact on the electrode surfaces compared to CDI, where scaling occurs in spacers and electrodes as depicted in Fig. 1c. This is attributed to the IEMs effectively hindering the movement of co-ions. Specifically, the AEM serves as a barrier to the transport of Ca^{2+} and Mg^{2+} ions towards the anode. Meanwhile, anions (HCO_3^- , PO_4^{3-} , and SO_4^{2-}) are hindered by the CEM from transporting towards the cathode, where Ca^{2+} and Mg^{2+} ions are electrosorbed [26,27]. In addition to Ca^{2+} and Mg^{2+} , other ions such as $\text{Fe}^{2+}/\text{Fe}^{3+}$ and Ba^{2+} can also precipitate, contingent on their concentrations, the presence of different counterions, and the pH of the feed water. Wang et al. examined Fe^{2+} scaling in MCDI, observing Fe^{2+} precipitation on both the AEM, CEM, and the spacer [27]. Despite this advancement, a comprehensive understanding of how changes in pH affect mineral scaling remains an unresolved aspect.

To address the challenges associated with mineral scaling in MCDI, this study systematically conducts desalination experiments using tap water and synthetic water. Effluent pH changes are recorded at various water recovery (WR) levels. These pH changes are elucidated by the removal of HCO_3^- ions and subsequent changes in the distribution of dissolved inorganic carbon (DIC) species. Furthermore, a mitigation

strategy is devised to mitigate mineral scaling by adjusting the thickness of the AEM.

2. Materials and methods

2.1. MCDI stack construction

The MCDI stack consisted of three cells, each comprising two graphitic current collectors, two activated carbon electrodes (PACMM 203, $\delta_e \sim 250 \mu\text{m}$, Material Methods, Irvine, CA, USA), a cation exchange membrane (CEM), an anion exchange membrane (AEM), and a porous spacer. The CEM (140 μm thick, Neosepta CMX, ASTOM Corporation, Tokyo, Japan) was positioned in front of the cathode, while the AEM (140 μm thick, Neosepta AMX, ASTOM Corporation, Tokyo, Japan) was in front of the anode. A nylon spacer (160 μm thick) was placed between the membranes. The graphite current collectors were situated behind each activated carbon electrode. To augment the thickness of the AEM within the stack, an extra AEM was placed in each cell.

2.2. Desalination experiments

Desalination experiments used three types of feed water: tap water (sourced from Wetsus, Leeuwarden, The Netherlands), synthetic water (prepared by dissolving NaCl , CaCl_2 , NaHCO_3 and CaCO_3 salts in deionized water), and a NaHCO_3 salt solution (prepared by dissolving NaHCO_3 salt in deionized water). Detailed ionic compositions are provided in Table S1. Water was circulated through the stack at a rate of 17 ml/min, achieving a productivity (P) of 55 L/h/m² at 50 % WR. To increase water recovery, the flow rate during discharge was reduced. Experiments were conducted in constant current (CC) mode using an Ivium-n-stat potentiostat (Ivium technologies, The Netherlands) with a current density of 11.1 A/m² during charging and reversed current during discharging. The half cycle time was 160 s, except for asymmetric experiments (see Section 2.2.3). Desalination experiments were performed at various water recovery conditions (WR, the ratio of desalinated water over the total volume of water treated) in single-pass mode (i.e., effluent water was drained). The pressure difference (Δp) between the stack inlet and outlet was continuously monitored using a differential pressure meter (EJA110E, Yokogawa Electric Corporation, Japan). Effluent pH and conductivity were also continuously recorded with 2-second data intervals using pH and conductivity sensors.

2.2.1. Feed water pH adjustment

In experiments involving tap water, the feed pH was measured at 7.73 ± 0.05 . However, in the case of the NaHCO_3 solution and synthetic tap water, the initial feed pH was higher than that of tap water and exhibited variability over time due to interactions with atmospheric CO_2 . To ensure a consistent comparison of pH changes during MCDI

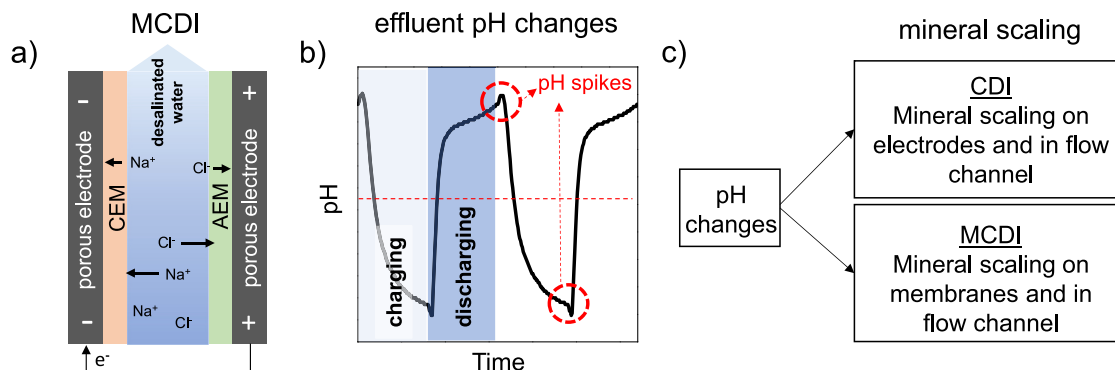


Fig. 1. (a) MCDI operation during the charging step, (b) the effluent pH during the desalination of a NaHCO_3 solution, and (c) the impact of pH changes in CDI and MCDI.

operation across different feed water compositions, we purged the NaHCO_3 solution and synthetic water with CO_2 to establish and maintain a stable feedwater pH of 7.73. Once $\text{pH} = 7.73$ was attained, it remained relatively stable (7.73 ± 0.03) throughout the experiment.

2.2.2. Sample collection and ionic composition analysis

In addition to continuous pH monitoring, we employed two methods for collecting desalinated water and concentrate samples. The first method involved sample collection throughout the entire charging or discharging step (i.e., 160 s), while the second method focused specifically on samples collected during the final 50 s of the charging or discharging step, representing the steady-state period. Following sample collection, we measured the pH and conductivity of each sample (within approximately 5 min). For the determination of cationic and anionic concentrations, we used inductively coupled plasma-optical emission spectroscopy (ICP-OES, Optima 5300 DV, PerkinElmer) and ion chromatography (IC, Dionex Aquion, Thermo Scientific), respectively. The bicarbonate ion concentration was calculated using Aqion software, employing charge and mass balance calculations involving all other measured ions.

2.2.3. Asymmetric desalination experiments

Experiments involving asymmetric desalination conditions, where variations occur between the charging and discharging steps, are conducted. In each experiment, parameters during the charging step, such as flow rate (17 ml/min for the stack), charging time (160 s), and current density (11.1 A/m^2 for the stack), remained constant. However, during the discharging step, only the flow rate remained constant, while the discharging time and current density were adjusted to ensure that the total charge transferred during the discharging step matched that of the charging step. Specific discharge conditions employed in asymmetric experiments are outlined in detail in Table S2.

2.3. Mineral scaling experiments

Mineral scaling experiments were conducted using two configurations of the MCDI stack: one with a single AEM (Single-AEM MCDI) and the other with double AEM (Double-AEM MCDI), as described in Section 2.1. For tap water, scaling experiments were conducted continuously for over 100 h of operation, while for synthetic water, they were carried out for a duration of 17.8 h (200 cycles). Throughout the scaling experiments, continuous measurement of the pressure difference (Δp) across the MCDI stack inlet and outlet was performed. Following each experiment, the stack underwent a cleaning process involving the circulation of a 0.1 M HCl solution through the stack until Δp returned to its initial value (± 10 mbar). This cleaning procedure, typically lasting 2–4 h, aimed to remove any scale formation and prepare the cell for subsequent experiments. After acid cleaning, the feed water was pumped through the cell until both the feed pH and effluent pH were equal.

2.4. Calculation of ionic composition, saturation index, DIC, and titration

Aqion Pro 8.1.5 software was used to compute the concentrations of the DIC species (H_2CO_3 , HCO_3^- , and CO_3^{2-}), as well as the Langelier saturation index (LSI) in both the feed water and the samples collected during charging and discharging. Additionally, titration curves for NaHCO_3 titration with an acid were generated using the software. These calculations were performed by taking into account charge and mass balance principles. The calculations were conducted for a closed CO_2 system, meaning there was no interaction with the atmosphere.

2.4.1. Ionic composition calculations for feed water

In the feed water, all ions except for carbonates are experimentally measured, along with pH. These measured concentrations and pH values are then input into the software to calculate the DIC concentration, including HCO_3^- and CO_3^{2-} . The calculations were performed employing

charge and mass balance principles, while assuming a closed CO_2 system.

2.4.2. Ionic composition & LSI calculations for collected samples

In analysing the ionic composition of collected samples, we used both the measured ionic concentrations and pH as fixed parameters to compute the concentrations of dissolved inorganic carbon (DIC). The pH measured experimentally in these collected samples represents the average pH of the total volume of desalinated or concentrate water collected during the entire step. Hence, the calculated DIC concentrations reflect the concentrations for the entire adsorption or desorption step, based on the measured pH. To account for varying pH values and their impact on ionic composition, different pH inputs were used, and a charge balance was conducted for each pH value to ascertain the corresponding ionic composition, including DIC concentrations. Additionally, these calculations facilitated the extraction of the Langelier Saturation Index (LSI) values for each sample from the software. The detailed calculation method of LSI is outlined in our previous study [25].

2.4.3. DIC calculation for NaHCO_3 desalination

The DIC concentration during NaHCO_3 desalination was calculated by using the effluent Na^+ concentration (calculated from effluent conductivity) and the effluent pH as inputs. With these inputs, the DIC concentration is calculated through charge and mass balances considering a closed system.

2.4.4. Titration calculations

To predict the titration curves in Aqion Pro, we input the concentrations of NaHCO_3 , and the charge balance is adjusted based on the DIC concentration before titrating against HCl (50 mM). The titration predictions take into account a closed CO_2 system, mirroring the conditions of experimental titrations conducted in a closed vessel.

3. Results and discussion

3.1. pH changes in MCDI

We conducted desalination experiments using tap water, a synthetic solution containing a limited set of salts (consisting of Na^+ , Ca^{2+} , Cl^- , and HCO_3^-), and a single salt solution (only Na^+ and HCO_3^-) to elucidate the underlying mechanisms of pH changes. As depicted in Fig. 2(a-c), the charging step induces a decrease in pH, while discharging leads to an increase in pH across all feed waters. Notably, the effluent pH changes demonstrate consistent trends in terms of both direction and dynamics for both the NaHCO_3 (single salt) solution and multi-ionic salt solutions (tap water, multi-ionic synthetic water). However, in previous work we have demonstrated that for single salt solutions, when the anion present is Cl^- instead of HCO_3^- , the resulting pH changes differ in terms of direction and dynamics, as demonstrated by the desalination of NaCl solution instead of NaHCO_3 , as shown in Fig. 2d.

This finding suggests that the presence of different anions in the water impacts the changes in effluent pH. The diverging trends in pH may stem from variations in anion compositions; specifically, the amphoteric nature of HCO_3^- allows it to function as both an acid and a base, influencing pH, whereas Cl^- does not buffer the solution pH. Previous research by Arulrajan et al. [25] has shown that, under identical experimental conditions (11.1 A/m^2 current density, feed water equilibrated with the atmosphere, and voltages below 0.95 V), faradaic reactions occur solely at pristine electrodes, and as electrodes age, pH changes are predominantly attributed to non-faradaic processes [25]. Hence, faradaic reactions can be discounted as a potential cause of pH changes, with focus instead on HCO_3^- ion adsorption and desorption as the primary driver in feed waters where these ions are present.

To investigate the impact of effluent concentration on pH changes, we conducted additional desalination experiments using freshly prepared NaHCO_3 with an initial feed pH of 8.35. By adjusting the applied

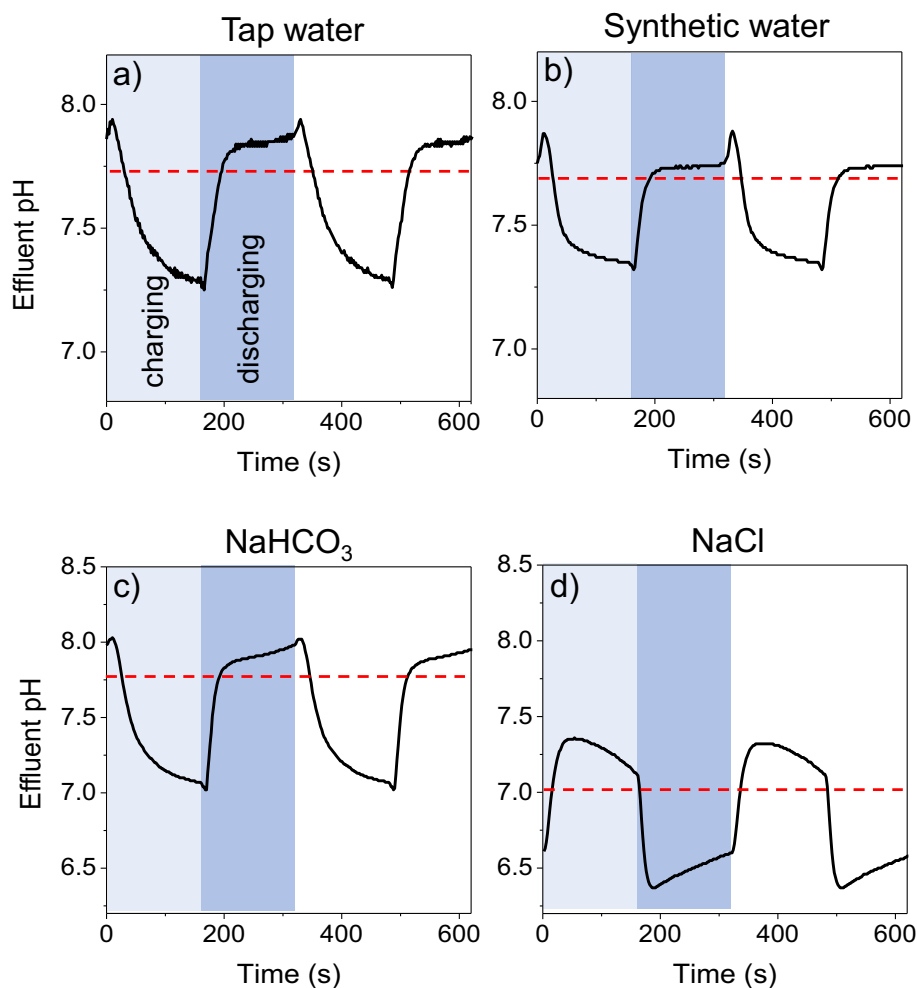


Fig. 2. Effluent pH changes observed during desalination of a) tap water, b) synthetic water, c) a NaHCO_3 solution and d) an NaCl solution (adapted from our previous study, Arulrajan et al. [25]). The feed pH of the NaCl solution is 7, while for all other feed waters the pH is 7.72.

current density to the MCDI stack, we adjusted the ion concentration in the effluent water (Δc). Fig. 3a presents the mean effluent pH during adsorption and desorption steps relative to the applied current density. As the charging current density increases from 4.95 A/m^2 to 8.9 A/m^2 , the effluent pH decreases from 8.31 to 8.26. Conversely, during discharge, the effluent pH rises from 8.41 to 8.46. This observation indicates that modifying the applied current density to alter ion concentrations in the effluent directly influences the magnitude of pH variations in tap water.

To understand the effect of operational parameters such as current density, which can affect the effluent concentration and subsequently pH changes, particularly for concentrates, we conducted asymmetric desalination experiments using tap water. Throughout these experiments, the conditions (i.e., flow rate, current density, and charging time) during the charging step remained the same across all experiments, but the conditions during the discharging step were varied (maintaining a constant flow rate while altering the current density and discharging times). In these asymmetric experiments, the change in effluent

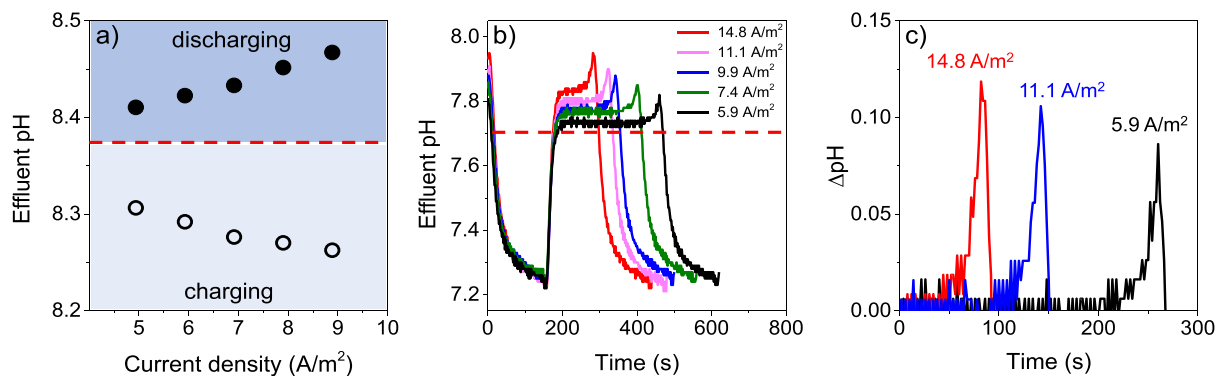


Fig. 3. (a) Averaged effluent pH of the experiment with the NaHCO_3 solution during charging and discharging, (b) the effluent pH changes during asymmetric desalination experiments, and (c) the magnitude of pH spikes at the beginning of the charging step.

concentration during charging remained consistent across all cycles due to the uniformity of experimental conditions, whereas the effluent concentration during discharging is affected by the applied current. The cell voltage during asymmetric experiments is presented in Fig. S1. When the current was increased during discharging, the discharging time was proportionally reduced to keep the total charge transferred during discharge the same for all applied currents. Fig. 3b shows the effluent pH during asymmetric desalination. The pH changes observed in different asymmetric experiments overlapped during the charging step, while during the discharging step, the magnitude of effluent pH changes increases with increasing current density. A noteworthy aspect of pH changes is the distinct pH spike at the beginning of the charging step, followed by a smaller yet inverted pH spike at the beginning of the discharging step, as shown in Fig. 2a-c. As illustrated in Fig. 3b, the magnitude of the pH spike during the charging step was influenced by the current density applied during charging, with higher current densities resulting in larger pH spikes. These pH spikes can induce mineral scaling, particularly when hardness ions are present at elevated concentrations.

3.2. pH changes with high DIC concentrations

To investigate the mechanisms causing pH changes, we focussed on a simpler solution than tap water, i.e., a NaHCO_3 solution. Despite the effluent pH fluctuations during charging and discharging, the effluent concentration stabilizes at a steady plateau value shortly after the start of a charging or discharging step (Fig. 4a), characteristic of constant current operation. The HCO_3^- ions, being amphoteric, participate in the carbonic acid equilibrium expressed as: $\text{H}_2\text{O} + \text{CO}_2(\text{g}) \rightleftharpoons \text{H}_2\text{CO}_3^* \rightleftharpoons \text{HCO}_3^- + \text{H}^+ \rightleftharpoons \text{CO}_3^{2-} + 2\text{H}^+$ (Apparent H_2CO_3^* represents the combined concentrations of H_2CO_3 and aqueous CO_2). This equilibrium governs the concentration of each species involved, including $\text{CO}_2(\text{g})$, DIC (H_2CO_3^* , HCO_3^- , and CO_3^{2-}), along with pH [28]. Throughout charging and discharging, the adsorption and desorption of charged DIC species affect the carbonic acid equilibrium, leading to a shift in pH [25].

We used Aqion Pro software to compute the DIC concentration from the effluent pH and Na^+ concentration, employing the methodology outlined in the materials and methods section. This analysis aims to elucidate changes in DIC species (CO_2 , H_2CO_3^* , HCO_3^- , and CO_3^{2-}) concentrations. Notably, we calculated the concentrations of apparent H_2CO_3^* , HCO_3^- , and CO_3^{2-} while treating the MCDI stack as a closed system (i.e., no CO_2 exchange with atmospheric air). In the pH range between 7 and 8, H_2CO_3^* and HCO_3^- emerge as the dominant DIC species, while the concentration of CO_3^{2-} is negligible, as shown in Fig. S2 and S3.

Fig. 4a displays the effluent pH and the NaHCO_3 concentration, while Fig. 4b shows the concentrations of H_2CO_3^* and HCO_3^- over time. Clearly, due to the adsorption and desorption of charged DIC in the porous carbon electrodes, the equilibrium between H_2CO_3^* and HCO_3^- is

shifted. This shift in chemical equilibrium impacts the solution pH, as shown in Fig. 4a. Specifically, during charging, the H_2CO_3^* concentration experiences a sharp initial decline from the feed concentration ($\sim 200 \mu\text{M}$ to $\sim 60 \mu\text{M}$), followed by gradual increase, ultimately returning to the initial feed water concentration ($200 \mu\text{M}$) by the end of the charging step. Similarly, during discharge, the H_2CO_3^* concentration undergoes a sharp increase (from $\sim 200 \mu\text{M}$ to $\sim 1 \text{mM}$), followed by a gradual decline, once again reaching the initial feed concentration ($200 \mu\text{M}$) by the end of the discharging step. The sharp changes in H_2CO_3^* concentration coincide with the pH spike at the onset of the charging step, while the sharp decrease aligns with the inverted pH spike at the beginning of the discharging step.

Fig. 4b shows that the rapid H_2CO_3^* concentration change at the beginning of discharging ($\sim 0.75 \text{mM}$) is approximately sixfold higher than the corresponding change during charging ($\sim 0.13 \text{mM}$). However, this notable concentration increase does not translate into a proportionately amplified pH spike during discharge. As NaHCO_3 solution is a buffered solution, it is important to consider the buffer range of this solution to evaluate the reason for the magnitude in pH changes. At the beginning of the discharging step, the effluent pH is 7.1, which is close to the pK_a (6.37) of the carbonic acid-bicarbonate equilibrium [29], indicating that the pH is minimally impacted by changes in the concentration of DIC species. At the beginning of the charging step, however, the effluent pH is 7.9, which is further away from the pK_a of 6.37, and is therefore in the poorly buffered pH range. This lower buffer capacity could be the reason for the more pronounced pH spike at the beginning of the charging step. This argument is supported by the calculation conducted for the titration of NaHCO_3 composition measured during discharge, see Fig. S7.

3.3. Mineral scaling in MCDI

The pH changes in MCDI can induce scaling, especially noticeable under high water recovery conditions ($\text{WR} > 50\%$) [30]. During the investigation of mineral scaling, we examined various water recovery conditions. Our focus was on assessing the impact of AEM thickness on mineral scaling, as membrane thickness can influence the flux ratio of different species [31]. Two configurations of MCDI stacks were employed: one with a single-AEM MCDI cell and the other with a double-AEM MCDI cell setup. Desalination experiments were conducted for durations exceeding 100 h for each water recovery condition. To enhance water recovery, the flow rate during discharge was reduced. Mineral scaling in the flow channel was monitored by continuously measuring the pressure difference (Δp) across the spacer channel during experiments [30].

The Δp measured between the inlet and outlet of the MCDI cell represents the pressure difference across the spacer channel connecting the inlet and outlet. Mineral scaling occurs when minerals precipitate, blocking pores in the spacer. This blockage leads to an increase in Δp . In

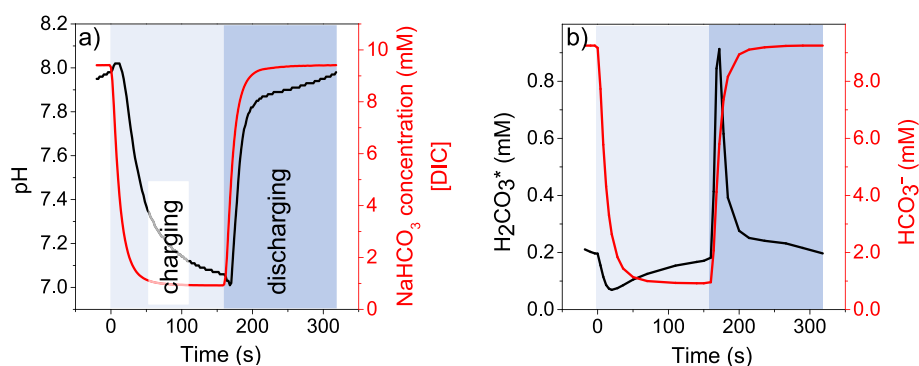


Fig. 4. (a) The effluent NaHCO_3 concentration and pH during charging and discharging of MCDI. (b) The calculated concentrations of two primary DIC species, namely HCO_3^- and H_2CO_3^* , during charging and discharging.

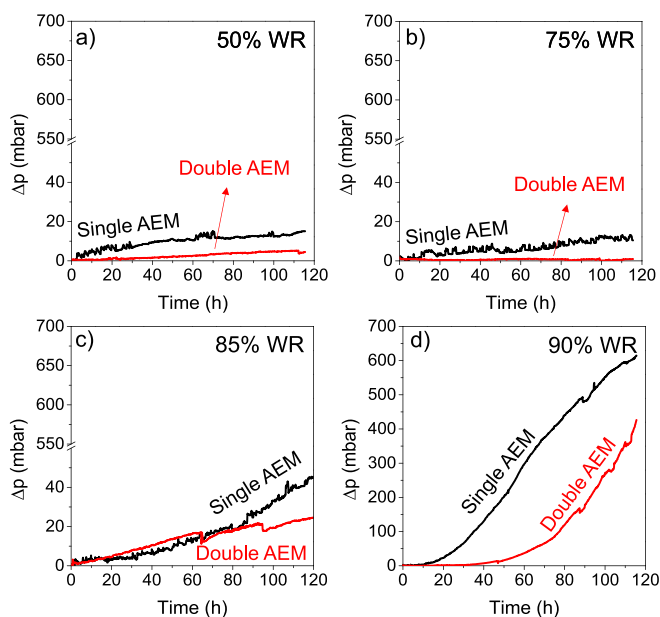


Fig. 5. Pressure difference, an indication for mineral scaling, across the MCDI cell against operational time during tap water desalination at water recoveries a) 50 %, b) 75 %, c) 85 %, d) 90 %.

MCDI systems, Δp values often serve as indicators prompting cleaning cycles for mineral scale removal. Typically, cleaning cycles commence just before Δp begins to rise exponentially; however, specifics vary between systems, lacking a standardized protocol for cleaning cycle initiation. In this study, a threshold of 100 mbar was set to compare mineral

scaling across operational conditions.

Fig. 5 shows that, for tap water desalination, an increase in Δp with time is observed, which is an indicator of mineral scaling. Notably, at 50 % and 75 % WR conditions, Δp remains relatively stable, with values below 20 mbar even after 110 h of operation. At 85 % WR, although scaling causes a more pronounced increase in Δp , it does not reach the threshold of 100 mbar during the experiment. Only at WR of 90 %, substantial Δp changes occur over time in both MCDI configurations. For the single-AEM MCDI, 100 mbar is reached in 35 h; whereas, with double-AEM MCDI, it takes ~ 80 h. This observation gives experimental support that increasing AEM thickness reduces mineral scaling, and therefore the consumption of cleaning in place chemicals.

Experiments with tap water were poorly reproducible. Subsequent examination upon MCDI stack disassembly revealed pronounced mineral scaling exclusively on the spacer as visibly depicted in Fig. S4, whereas IEMs remained largely unaffected. The precipitated salt in the spacer was subjected to Raman spectral analysis. The Raman analysis shows 4 distinctive peaks at 153, 280, 712 and 1085 cm^{-1} which are in line with the peaks for calcite (CaCO_3) revealing that the precipitated mineral is calcite, see Fig. S5 [32]. Interestingly, the initially transparent AEMs exhibited a brown hue (as seen in Fig. S6), potentially attributable to organic adsorption (e.g., humic/fluvic acid substances). This membrane fouling could impair experimental reproducibility. Therefore, we studied scaling in synthetic water containing only Na^+ and Ca^{2+} cations, and Cl^- and $\text{HCO}_3^-/\text{CO}_3^{2-}$ anions, with increased Ca^{2+} ion concentrations to accelerate mineral scaling (Table S1). These synthetic water scaling experiments were carried out for 200 desalination cycles (equivalent to ~ 18 h), repeated three times for 85 % and 90 % WR to ensure replicability.

Fig. 6 shows Δp changes over operational time for synthetic water. Similar to the trends observed in tap water mineral scaling, experiments with synthetic water also demonstrate an increase in scaling with rising

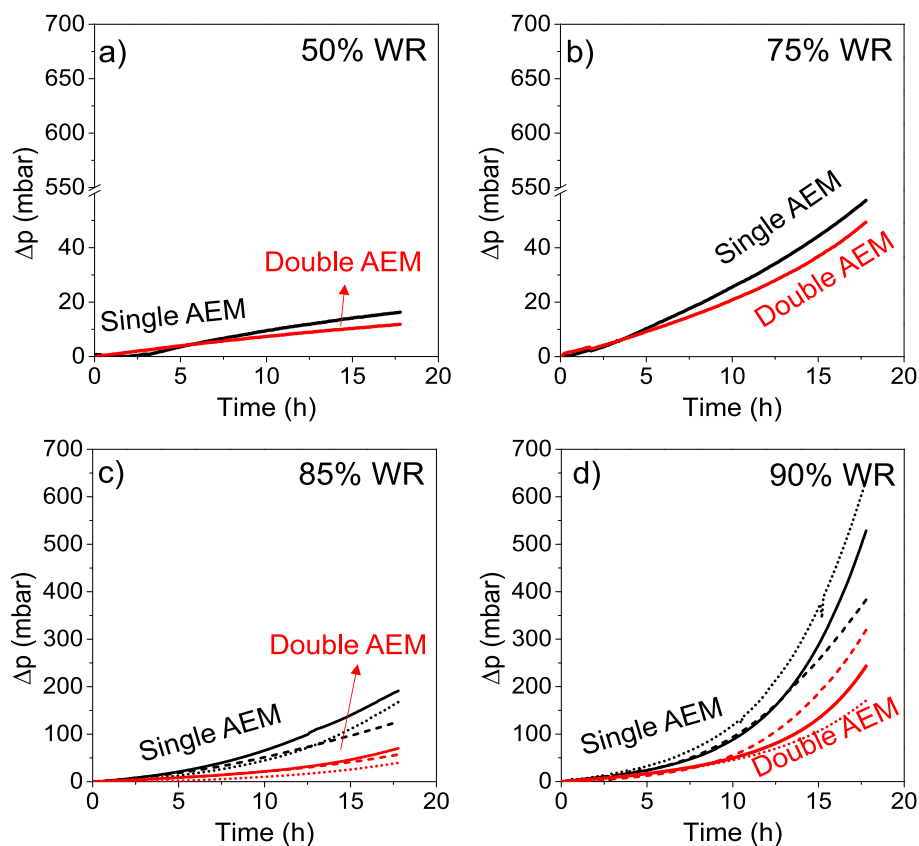


Fig. 6. Pressure difference across the MCDI cell against operational time as an indication for mineral scaling during synthetic water desalination at water recoveries a) 50 %, b) 75 %, c) 85 %, d) 90 %. The dotted and solid lines of the same colour show data from replicate experiments.

WR. However, at 50 % and 75 % WR, though Δp increases it does not reach the 100 mbar threshold within the ~18-hour operational timeframe. At 85 % WR, the single-AEM MCDI stack reaches 100 mbar Δp in 14 h, while the double-AEM MCDI stack does not reach the 100 mbar threshold within the operational timeframe. Upon increasing the WR to 90 %, the single-AEM MCDI achieves a 100 mbar Δp in 10 h, whereas the double-AEM MCDI stack takes 13.5 h, displaying that scaling is approximately 1.35 times slower. In experiments with tap water and synthetic water, mineral scaling is primarily influenced by two factors: the hardness ion concentration (Ca^{2+} , Mg^{2+}) and pH. Analysis of ionic composition in tap water experiments shows no significant difference between single AEM and double AEM configurations. Effluent pH data from tap water and synthetic water experiments alone cannot explain pH variations by the AEM thickness, as simultaneous scaling can impact the measured effluent pH. To address this, we conducted theoretical calculations of the Langelier Saturation Index (LSI). The LSI is an indicator that shows the extent of scaling potential of a solution based on pH, TDS (total dissolved solids), temperature, Ca^{2+} concentration and alkalinity. While desalinating tap water or artificial tap water, at higher WR, the concentration of Ca^{2+} ions (together with all other ions) and pH in the effluent increases. This results in the precipitation of CaCO_3 (calcite) on the spacer. When the LSI values are above 0.5, the potential for scaling is significantly high. We calculated the LSI for the concentrate composition of 90 % water recovery under two conditions: firstly, varying the Ca^{2+} concentration (and Na^+ concentration to maintain the charge balance) with constant pH, and secondly, varying pH and the total DIC concentration while the other ionic concentrations are constant, see Fig. S8. The initial LSI value for the concentrate is 1, and to raise the LSI to 1.2, the Ca^{2+} concentration must increase by 73 % (i.e., from 3.42 mM to 5.92 mM) when pH is fixed, while a 2.9 % increase in pH (i.e., from 8.02 to 8.25) results in the same LSI with fixed concentrations of Ca^{2+} and of the other ions except DIC. As the difference in the Ca^{2+} concentration between single AEM and CEM experiments is not significant (i.e., only 8.75 %), the difference in effluent pH between single and double AEM is probably the most important cause of the observed differences in scaling, as shown in Figs. 5 and 6.

4. Conclusion

We conducted a series of experiments to understand the mechanisms driving pH changes during desalination processes, focusing on solutions containing HCO_3^- ions (such as tap water, synthetic water and NaHCO_3). Our empirical findings demonstrate that pH changes observed in NaHCO_3 experiments directly result from HCO_3^- removal, which we identify as a significant mechanism driving pH changes in tap water. Through systematic experiments and calculations, we determined that HCO_3^- removal, along with changes in concentrations of other dissolved inorganic carbon (DIC) species, can lead to pH changes by altering the carbonic acid equilibrium. Furthermore, we observed that desalination of tap water or synthetic water containing hardness ions at higher WR conditions results in elevated pH levels, contributing to increased mineral scaling. Raman spectral analysis revealed that during tap water desalination, scaling primarily occurs due to the precipitation of calcite mineral. Our findings also demonstrate that increasing the thickness of the AEM can reduce mineral scaling in MCDI, consequently decreasing the need for anti-scaling agents.

CRedit authorship contribution statement

Antony Cyril Arulrajan: Writing – review & editing, Writing – original draft, Validation, Software, Methodology, Investigation, Formal analysis, Data curation, Conceptualization. **Min-Chen Wu:** Writing – review & editing, Validation, Investigation, Formal analysis. **Slawomir Porada:** Writing – review & editing, Supervision, Resources, Project administration, Conceptualization. **Jouke E. Dykstra:** Writing – review & editing, Supervision, Resources, Project administration,

Conceptualization. **Chia-Hung Hou:** Writing – review & editing, Supervision, Resources. **Albert van der Wal:** Writing – review & editing, Supervision, Resources, Project administration, Funding acquisition, Conceptualization.

Declaration of competing interest

The authors declare that they have no known competing financial interests or personal relationships that could have appeared to influence the work reported in this paper.

Data availability

Data will be made available on request.

Acknowledgement

This work was performed in the cooperation framework of Wetsus, European Centre of Excellence for Sustainable Water Technology (www.wetsus.nl). Wetsus is cofunded by the Dutch Ministry of Economic Affairs and Ministry of Infrastructure and Environment, the European Union Regional Development Fund, the Province of Fryslân, and the Northern Netherlands Provinces. This work is partly received funding from the European Union's Horizon 2020 research and innovation programme under the Marie Skłodowska-Curie grant agreement No 665874 and partly funded by the National Science Centre, Poland [2022/01/1/ST5/00025] and the Polish National Agency for Academic Exchange [Polish Returns grant BPN/PPO/2021/1/00010]. The authors thank the participants of the Wetsus research theme “Desalination and Concentrates” for fruitful discussions and financial support. Jouke E. Dykstra acknowledges the support by the Netherlands Organisation for Scientific Research (NWO), Domain Applied and Engineering Science (TTW), and the Ministry of Economic Affairs (VENIgrant no 19111).

Appendix A. Supplementary data

Supplementary data to this article can be found online at <https://doi.org/10.1016/j.jwpe.2024.105094>.

References

- [1] J. El Kharraz, A. El-Sadek, N. Ghaffour, E. Mino, Water scarcity and drought in WANA countries, *Procedia Eng.* 33 (2012) 14–29, <https://doi.org/10.1016/j.proeng.2012.01.1172>.
- [2] V.G. Gude, Desalination and sustainability – an appraisal and current perspective, *Water Res.* 89 (2016) 87–106, <https://doi.org/10.1016/j.watres.2015.11.012>.
- [3] A.E. Ercin, A.Y. Hoekstra, Water footprint scenarios for 2050: a global analysis, *Environ. Int.* 64 (2014) 71–82, <https://doi.org/10.1016/j.envint.2013.11.019>.
- [4] S.-Y. Pan, A.Z. Haddad, A. Kumar, S.-W. Wang, Brackish water desalination using reverse osmosis and capacitive deionization at the water-energy nexus, *Water Res.* 183 (2020) 116064, <https://doi.org/10.1016/j.watres.2020.116064>.
- [5] Y. Le Gouellec, Calcium sulfate (gypsum) scaling in nanofiltration of agricultural drainage water, *J. Membr. Sci.* 205 (2002) 279–291, [https://doi.org/10.1016/S0376-7388\(02\)00128-X](https://doi.org/10.1016/S0376-7388(02)00128-X).
- [6] D. Zhou, L. Zhu, Y. Fu, M. Zhu, L. Xue, Development of lower cost seawater desalination processes using nanofiltration technologies – a review, *Desalination* 376 (2015) 109–116, <https://doi.org/10.1016/j.desal.2015.08.020>.
- [7] I.J. Esfahani, J. Rashidi, P. Ifaei, C.K. Yoo, Efficient thermal desalination technologies with renewable energy systems: a state-of-the-art review, *Korean J. Chem. Eng.* 33 (2016) 351–387, <https://doi.org/10.1007/s11814-015-0296-3>.
- [8] M.E. Suss, S. Porada, X. Sun, P.M. Biesheuvel, J. Yoon, V. Presser, Water desalination via capacitive deionization: what is it and what can we expect from it? *Energy Environ. Sci.* 8 (2015) 2296–2319, <https://doi.org/10.1039/c5ee00519a>.
- [9] S. Al-Amshawe, M.Y.B.M. Yunus, A.A.M. Azoddein, D.G. Hassell, I.H. Dakhil, H. A. Hasan, Electrodialysis desalination for water and wastewater: a review, *Chem. Eng. J.* 380 (2020) 122231, <https://doi.org/10.1016/j.cej.2019.122231>.
- [10] A.E. Al-Rawajfeh, H. Glade, J. Ulrich, Scaling in multiple-effect distillers: the role of CO₂ release, *Desalination* 182 (2005) 209–219, <https://doi.org/10.1016/j.desal.2005.04.013>.
- [11] A.J. Karabelas, S.T. Mitrouli, M. Kostoglou, Scaling in reverse osmosis desalination plants: a perspective focusing on development of comprehensive simulation tools, *Desalination* 474 (2020) 114193, <https://doi.org/10.1016/j.desal.2019.114193>.

- [12] A. Matin, F. Rahman, H.Z. Shafi, S.M. Zubair, Scaling of reverse osmosis membranes used in water desalination: phenomena, impact, and control; future directions, *Desalination* 455 (2019) 135–157, <https://doi.org/10.1016/j.desal.2018.12.009>.
- [13] M. Al-Shammiri, M. Ahmed, M. Al-Rageeb, Nanofiltration and calcium sulfate limitation for top brine temperature in Gulf desalination plants, *Desalination* 167 (2004) 335–346, <https://doi.org/10.1016/j.desal.2004.06.143>.
- [14] J. Choi, H. Lee, S. Hong, Capacitive deionization (CDI) integrated with monovalent cation selective membrane for producing divalent cation-rich solution, *Desalination* 400 (2016) 38–46, <https://doi.org/10.1016/j.desal.2016.09.016>.
- [15] Z. Zhang, S.S. Wadekar, O.R. Lokare, R.D. Vidic, Comparison of calcium scaling in direct contact membrane distillation (DCMD) and nanofiltration (NF), *J. Membr. Sci.* 638 (2021) 119647, <https://doi.org/10.1016/j.memsci.2021.119647>.
- [16] E. Ayala-Bribiesca, M. Araya-Farias, G. Pourcelly, L. Bazinet, Effect of concentrate solution pH and mineral composition of a whey protein diluate solution on membrane fouling formation during conventional electrodialysis, *J. Membr. Sci.* 280 (2006) 790–801, <https://doi.org/10.1016/j.memsci.2006.02.036>.
- [17] Q. Liu, G.-R. Xu, R. Das, Inorganic scaling in reverse osmosis (RO) desalination: mechanisms, monitoring, and inhibition strategies, *Desalination* 468 (2019) 114065, <https://doi.org/10.1016/j.desal.2019.07.005>.
- [18] C. Gabrielli, G. Maurin, G. Poindessous, R. Rosset, Nucleation and growth of calcium carbonate by an electrochemical scaling process, *J. Cryst. Growth* 200 (1999) 236–250, [https://doi.org/10.1016/S0022-0248\(98\)01261-5](https://doi.org/10.1016/S0022-0248(98)01261-5).
- [19] F. Yu, L. Wang, Y. Wang, X. Shen, Y. Cheng, J. Ma, Faradaic reactions in capacitive deionization for desalination and ion separation, *J. Mater. Chem. A* 7 (2019) 15999–16027, <https://doi.org/10.1039/c9ta01264h>.
- [20] C.A.C. van de Lisdonk, J.A.M. van Paassen, J.C. Schippers, Monitoring scaling in nanofiltration and reverse osmosis membrane systems, *Desalination* 132 (2000) 101–108, [https://doi.org/10.1016/S0011-9164\(00\)00139-9](https://doi.org/10.1016/S0011-9164(00)00139-9).
- [21] W. Tang, D. He, C. Zhang, P. Kovalsky, T.D. Waite, Comparison of Faradaic reactions in capacitive deionization (CDI) and membrane capacitive deionization (MCDI) water treatment processes, *Water Res.* 120 (2017) 229–237, <https://doi.org/10.1016/j.watres.2017.05.009>.
- [22] C. Zhang, D. He, J. Ma, W. Tang, T.D. Waite, Faradaic reactions in capacitive deionization (CDI) - problems and possibilities: a review, *Water Res.* 128 (2018) 314–330, <https://doi.org/10.1016/j.watres.2017.10.024>.
- [23] J.E. Dykstra, K.J. Keesman, P.M. Biesheuvel, A. van der Wal, Theory of pH changes in water desalination by capacitive deionization, *Water Res.* 119 (2017) 178–186, <https://doi.org/10.1016/j.watres.2017.04.039>.
- [24] S. Porada, R. Zhao, A. van der Wal, V. Presser, P.M.M. Biesheuvel, Review on the science and technology of water desalination by capacitive deionization, *Prog. Mater. Sci.* 58 (2013) 1388–1442, <https://doi.org/10.1016/j.pmatsci.2013.03.005>.
- [25] A.C. Arulrajan, J.E. Dykstra, A. van der Wal, S. Porada, Unravelling pH changes in electrochemical desalination with capacitive deionization, *Environ. Sci. Technol.* 55 (2021), <https://doi.org/10.1021/acs.est.1c04479> (acs.est.1c04479).
- [26] T. Wang, C. Zhang, L. Bai, B. Xie, Z. Gan, J. Xing, G. Li, H. Liang, Scaling behavior of iron in capacitive deionization (CDI) system, *Water Res.* 171 (2020) 115370, <https://doi.org/10.1016/j.watres.2019.115370>.
- [27] T. Wang, L. Bai, C. Zhang, X. Zhu, J. Xing, Y. Guo, J. Wang, D. Lin, G. Li, H. Liang, Formation mechanism of iron scale in membrane capacitive deionization (MCDI) system, *Desalination* 495 (2020) 114636, <https://doi.org/10.1016/j.desal.2020.114636>.
- [28] J.J. Cole, Y.T. Prairie, Dissolved CO₂ in freshwater systems, in: *Ref. Modul. Earth Syst. Environ. Sci.*, Elsevier, 2014, pp. 1–5, <https://doi.org/10.1016/b978-0-12-409548-9.09399-4>.
- [29] D. Pines, J. Ditkovich, T. Mukra, Y. Miller, P.M. Kiefer, S. Daschakraborty, J. T. Hynes, E. Pines, How acidic is carbonic acid? *J. Phys. Chem. B* 120 (2016) 2440–2451, <https://doi.org/10.1021/acs.jpcc.5b12428>.
- [30] M. Mossad, L. Zou, Study of fouling and scaling in capacitive deionisation by using dissolved organic and inorganic salts, *J. Hazard. Mater.* 244–245 (2013) 387–393, <https://doi.org/10.1016/j.jhazmat.2012.11.062>.
- [31] T.M. Mubita, S. Porada, P.M. Biesheuvel, A. van der Wal, J.E. Dykstra, Strategies to increase ion selectivity in electrodialysis, *Sep. Purif. Technol.* 292 (2022) 120944, <https://doi.org/10.1016/j.seppur.2022.120944>.
- [32] F.C. Donnelly, F. Purcell-Milton, V. Framont, O. Cleary, P.W. Dunne, Y.K. Gun'ko, Synthesis of CaCO₃ nano- and micro-particles by dry ice carbonation, *Chem. Commun.* 53 (2017) 6657–6660, <https://doi.org/10.1039/C7CC01420A>.